I atoms are produced at the $\omega_3 = 3\omega_1$ energy level (at ~10.6 eV). This signature is also evident in the modulation data. Between 354.98 and 356.18 nm, which corresponds to the region of the $5d\pi$ and $5d\delta$ resonances of HI (*20*), we obtained control with a 150° lag between the two signals. Between 354.28 and 354.88 nm (the region of the $5f\sigma$ and $5f\pi$ resonances), we saw little or no modulation of the ion signals, while between 353.78 and 354.23 nm (the region of the $5s\sigma$ resonance) we again obtained modulation, but in this case there was no lag between the HI^+ and I^+ signals. Finally, for wavelengths shorter than 353.78 nm, modulation was again absent.

In order to obtain phase modulation of I^+, the controlled state must be reached by both ω_3 and $3\omega_1$. Because HI autoionization structure dominates the ω_3 spectrum of I^+ (Fig. 4B), it follows that I atoms are produced by ω_3 and $3\omega_1$ at 10.6 eV (*21*). This evidence rules out the second mechanism, which produces I at the $2\omega_1$ level. Moreover, the autoionizing structure of $I(^2P_{3/2})$ is absent in the I^+ spectrum (Fig. 1B). In particular, a strong resonance at the atomic ionization threshold (*22*) is conspicuously absent in this spectrum. Also, tuning the UV laser to the 2+1 REMPI frequencies of $I(^2P_{1/2,\ 3/2})$ failed to produce any structure in the I^+ spectrum (Fig. 1B). If two photons produce an excess of I atoms, both of these features would be prominent in the spectrum.

Another possibility involving two sequential control steps (for example, reactions 7 and 9) can be also ruled out, because this mechanism would cause I^+ to have twice the modulation frequency of HI^+.

We have controlled the outcome of a chemical reaction by quantum-mechanical interference between competing excitation paths. We have used two laser beams to promote the HI molecule to a state that is embedded in both autoionization and predissociation continua. By varying the phase difference between the two beams we favor one reaction product over the other. The ultimate goal of using lasers to break specific bonds in a molecule appears to be within reach.

REFERENCES AND NOTES

1. E. Jensen *et al.*, *J. Chem. Phys.* **98**, 1882 (1993).
2. W. S. Warren, H. Rabitz, M. Dahleh, *Science* **259**, 1581 (1993); S. A. Rice, *ibid.* **258**, 412 (1992).
3. R. Kosloff, S. A. Rice, P. Gaspard, S. Tersigni, D. J. Tannor, *Chem. Phys.* **139**, 201 (1989).
4. T. Baumert, M. Grosser, R. Thalweiser, G. Gerber, *Rev. Phys. Lett.* **67**, 3753 (1991).
5. C. K. Chan *et al.*, *J. Chem. Phys.* **94**, 2688 (1991); A. D. Bandrauk, J. Gauthier, F. J. McCann, *ibid.* **100**, 340 (1994); M. Shapiro and P. Brumer, *ibid.* **84**, 4103 (1986); T. Nakajima, P. Lambropoulos, S. Cavalieri, M. Matera, *Phys. Rev. A* **46**, 7315 (1992).
6. T. Nakajima and P. Lambropoulos, *Phys. Rev. Lett.* **70**, 1081 (1993); *Phys. Rev. A* **50**, 595 (1994).
7. H. G. Muller, P. H. Bucksbaum, D. W. Schumacher, A. Zavriyev, *J. Phys. B* **23**, 2761 (1990).
8. C. Chen, Y.-Y. Yin, D. S. Elliott, *Phys. Rev. Lett.* **64**, 507 (1990); C. Chen and D. S. Elliott, *ibid.* **65**, 1737 (1990).
9. S. M. Park, S.-P. Lu, R. J. Gordon, *J. Chem. Phys.* **94**, 8622 (1991).
10. S. Lu, S. M. Park, Y. Xie, R. J. Gordon, *ibid.* **96**, 6613 (1992).
11. Y.-Y. Yin, C. Chen, D. S. Elliott, *Phys. Rev. Lett.* **69**, 2353 (1992); Y.-Y. Yin, D. S. Elliott, R. Shehadeh, E. R. Grant, *Chem. Phys. Lett.* **241**, 591 (1995).
12. V. Kleiman, L. Zhu, X. Li, R. J. Gordon, *J. Chem. Phys.* **102**, 5863 (1995).
13. M. Bjorklund, *IEEE J. Quant. Electron.* **QE-11**, 287 (1975).
14. R. J. Gordon *et al.*, *J. Chem. Phys.* **98**, 9481 (1993).
15. S. G. Tilford, M. L. Ginter, A. N. Bass, *J. Mol. Spectrosc.* **34**, 327 (1970).
16. G. N. A. Van Veen, K. A. Mohamed, T. Baller, A. E. de Vries, *Chem. Phys.* **80**, 113 (1983).
17. K. Huber and G. Herzberg, *Molecular Spectra and Molecular Structure* (Van Nostrand Reinhold, New York, 1979), vol. 4; N. Böwering, H. Klausing, M. Müller, M. Salzmann, U. Heinzmann, *Chem. Phys. Lett.* **189**, 467 (1992); S. Pratt, *J. Chem. Phys.* **101**, 8302 (1994).
18. C. J. Zietkiewicz, Y.-Y. Gu, A. M. Farkas, J. G. Eden, *J. Chem. Phys.* **101**, 86 (1994).
19. I. Levy and M. Shapiro, *ibid.* **89**, 2900 (1988).
20. J. H. D. Eland and J. Berkowitz, *ibid.* **67**, 5034 (1977); D. J. Hart and J. W. Hepburn, *Chem. Phys.* **129**, 51 (1989).
21. From Fig. 4, we know that the state reached with one VUV photon produces both HI^+ and I atoms. The ratio of HI^+ to I produced from this state is independent of the VUV intensity, and therefore applies equally to the spectra in Figs. 1 and 4. We also expect that the ratios of HI^+ to I produced from this level by one and three photons are approximately equal. Under the conditions of coherent control (that is, the conditions of Fig. 1) the concentrations of HI^+ produced by one and three photons are approximately equal. It follows that under the conditions of coherent control the concentrations of I produced by one and three photons are also approximately equal. We therefore conclude that the Rydberg structure, which dominates the one-photon spectrum in Fig. 4, is also present in the three-photon spectrum, although it is not readily visible at the poor signal-to-noise ratio of Fig. 1. It is still possible that under the conditions of coherent control there is also a contribution to the total I^+ signal generated at the two-photon level. Because the phase dependence of the controlled signal is tied to the Rydberg structure of HI, it is evident that the two-photon contribution is minor.
22. J. Berkowitz, C. H. Batson, G. L. Goodman, *Phys. Rev. A* **24**, 149 (1981); F. Robicheux and C. H. Greene, *ibid.* **46**, 3821 (1992).

23. We thank H. Lefebvre-Brion for many helpful discussions and the National Science Foundation for its support.

15 June 1995; accepted 24 July 1995

Radar Images of Asteroid 4179 Toutatis

Steven J. Ostro,* R. Scott Hudson, Raymond F. Jurgens, Keith D. Rosema, Donald B. Campbell, Donald K. Yeomans, John F. Chandler, Jon D. Giorgini, Ron Winkler, Randy Rose, S. Denise Howard, Martin A. Slade, Phil Perillat, Irwin I. Shapiro

Delay-Doppler images of the Earth-crossing asteroid 4179 Toutatis achieve resolutions as fine as 125 nanoseconds (19 meters in range) and 8.3 millihertz (0.15 millimeter per second in radial velocity) and place hundreds to thousands of pixels on the asteroid, which appears to be several kilometers long, topographically bifurcated, and heavily cratered. The image sequence reveals Toutatis to be in an extremely slow, non–principal axis rotation state.

Optical investigations of Earth-orbit–crossing asteroids (ECAs) are limited by their small angular sizes (typically $\ll$1 arc sec), but radar measurements of the distribution of echo power in time delay and Doppler frequency can be used to synthesize images of these objects. Toutatis's approach to within 0.024 astronomical unit (AU) (9.4 lunar distances) on 8 December 1992 was an unprecedented opportunity for radar investigation of a small body. We present images that achieve areal resolutions ~100 times finer than previously obtained (*1*) for any ECA and reveal an object with startling characteristics.

The images were obtained with the Goldstone Radar in California daily from 2 to 18 December and at the Arecibo Observatory in Puerto Rico daily from 14 to 19 December (Table 1). We used binary-phase coded wave forms (*2*) that provided a time resolution Δt equal to the temporal extent of each code element, a range resolution equal to Δt times half the speed of light, and a frequency resolution

$$\Delta f = 1/(RP \times N_{COH} \times L_{FFT}) = 1/T_{COH} \quad (1)$$

where the code repetition period RP equals Δt times the number of elements in the code (255 for Goldstone, 8191 for Arecibo) and N_{COH} is the number of successive, RP-

S. J. Ostro, R. F. Jurgens, K. D. Rosema, D. K. Yeomans, J. D. Giorgini, R. Winkler, R. Rose, S. D. Howard, M. A. Slade, Jet Propulsion Laboratory, California Institute of Technology, Pasadena, CA 91109–8099, USA.
R. S. Hudson, School of Electrical Engineering and Computer Science, Washington State University, Pullman, WA 99164–2752, USA.
D. B. Campbell, National Astronomy and Ionosphere Center, Space Sciences Building, Cornell University, Ithaca, NY 14853–6801, USA.
J. F. Chandler and I. I. Shapiro, Center for Astrophysics, 60 Garden Street, Cambridge, MA 02138, USA.
P. Perillat, Arecibo Observatory, Box 995, Arecibo, Puerto Rico 00613, USA.

*To whom correspondence should be addressed at mail stop 300-233. E-mail: ostro@echo.jpl.nasa.gov

long time series of decoded voltage samples that are coherently summed before spectral analysis with a fast Fourier transform of length L_{FFT} (256 for Goldstone, 2048 for Arecibo). A power spectral estimate for each delay "bin" is obtained from coherent analysis of T_{COH} seconds of data; we refer to such an image as one "look." Spectral estimation noise (3) is chi-square distributed and the fractional root-mean-square (rms) fluctuation in a sum of N looks is $N^{-1/2}$. Thus, fine frequency resolution requires a long coherence time T_{COH}, and low noise requires incoherent summation of many looks. However, long integrations are undesirable if the resolution is degraded by smearing from either the target's rotation or its translational motion with respect to the delay-Doppler prediction ephemeris, which is used to drift the sampling time base to maintain coregistration of echoes from any given range bin and to tune the receiver to the Doppler-shifted echo. The Doppler-prediction error $\Delta\nu_{eph}$ defines the rate of change of the delay-prediction error $\Delta\tau_{eph}$ and hence the rate of delay smearing

$$\frac{d\Delta\tau_{eph}(t)}{dt} = \frac{-\Delta\nu_{eph}(t)}{F_{TX}} \qquad (2)$$

where F_{TX} is the transmitter frequency. Our observations progressed through several generations of increasingly accurate ephemerides (Table 1).

Figure 1 shows our Goldstone 0.5-μs images and Arecibo 0.2-μs images (4). These images are very different from optical pictures. Constant-Doppler planes are parallel to both the line of sight (LOS) and the target's apparent spin vector, and constant-delay planes are normal to the LOS. These two orthogonal sets of planes cut the target into rectangular cells, and each image pixel shows the sum of echo power in one cell. Beyond the leading edge, each cell can capture echoes from surface regions on either side of the apparent equator, so the surface-to-image mapping is potentially two-to-one or even many-to-one. Moreover, the kilometers-per-hertz conversion factor for any image depends on the asteroid's apparent spin vector, as follows. For a rigid body whose center of mass (COM) is at a constant distance from the radar, the Doppler frequency of the echo from a point $\mathbf{r}$ with respect to the COM is

$$\nu = \frac{(\mathbf{W}_{app} \times \mathbf{r})\cdot\mathbf{e}}{(\lambda/2)} \qquad (3)$$

where the unit vector $\mathbf{e}$ points from the COM to the radar and we ignore parallax and second-order terms. The target's apparent spin vector $\mathbf{W}_{app}$ satisfies

$$\mathbf{W}_{app} = \mathbf{W} + \mathbf{W}_{sky} \qquad (4)$$

where $\mathbf{W}$ is the intrinsic spin vector and $\mathbf{W}_{sky}$ is the contribution from the target's plane-of-sky (POS) motion (Table 1). The kilometers-per-hertz conversion factors are

$$\text{Goldstone: } 87.2/|\mathbf{W}_{app} \times \mathbf{e}| = P/(4.13\cos\delta) \qquad (5)$$

$$\text{Arecibo: } 312/|\mathbf{W}_{app} \times \mathbf{e}| = P/(1.15\cos\delta) \qquad (6)$$

where spin rates are in degrees per day, $P = 360/|\mathbf{W}_{app}|$ is the instantaneous, apparent spin period in days, and $\delta = \cos^{-1}(|\mathbf{W}_{app} \times \mathbf{e}|/|\mathbf{W}_{app}|)$ is the instantaneous, apparent, target-centered declination of the radar.

The following discussion focuses on the Goldstone images. The distribution of echo power is extremely bimodal in most images (two lobes were perceptible even on 3, 7, 14, and 17 December, when they were at similar ranges and overlap), indicating a prominent bifurcation in Toutatis's shape. On 5 to 6 and 15 to 16 December, the lobes' central frequencies were similar and the large lobe was between the radar and the small lobe. No eclipse of the small lobe was evident, so a POS view of the asteroid would be expected to show both lobes. However, during 10 to 12 December, when the small lobe was closer, the large lobe's limb extended several microseconds further at frequencies not shared by the small lobe than it did at frequencies containing echoes from both lobes, indicating partial occultation of the large lobe by the small lobe. The 11 December image also shows the echo's greatest delay depth. Thus it appears that the lobe-lobe line coincided approximately with the asteroid's longest dimension and that both were closer to the LOS on 11 December than on any other date. The delay dispersions of the two components' echoes place lower bounds of 0.9 and 1.9 km on their maximum overall dimensions, but further interpretation of the images requires knowledge of the kilometers-per-

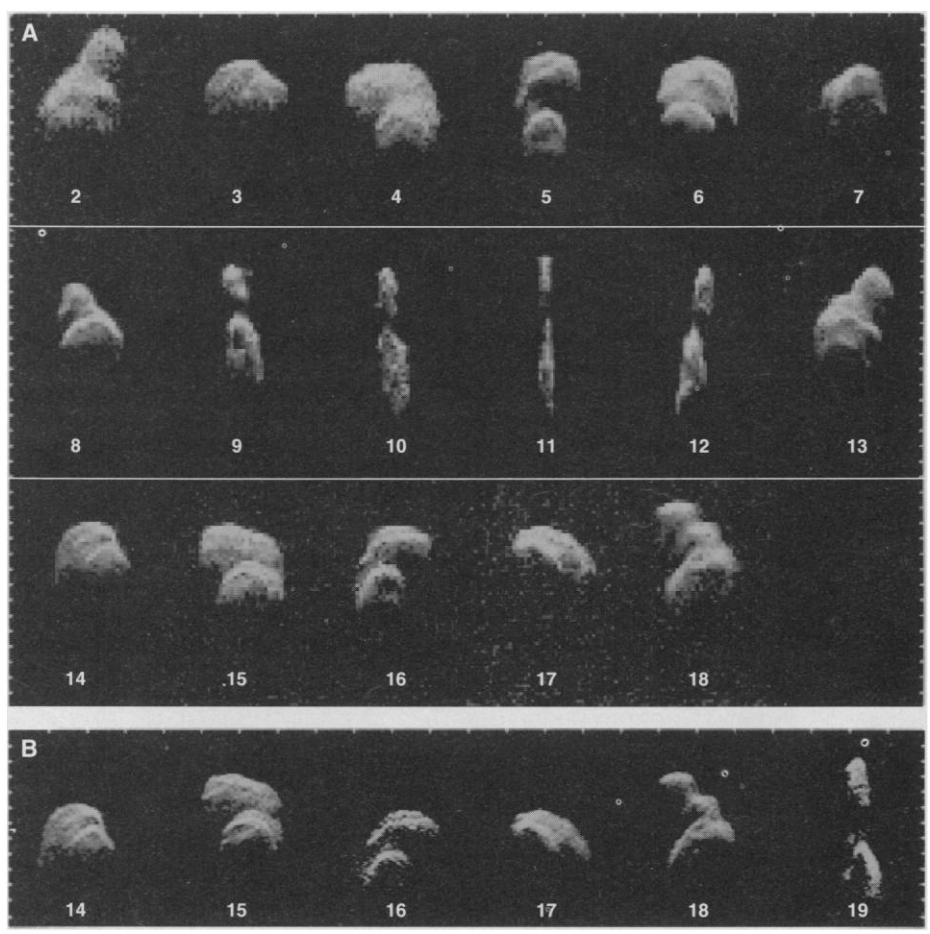

Fig. 1. Toutatis radar images (Table 1). (**A**) Goldstone low-resolution images and (**B**) Arecibo images plotted with time delay increasing toward the bottom and Doppler frequency increasing toward the left. Numbers indicate the date in December 1992. On the vertical sides, ticks are 2 μs apart. Two horizontal sides have ticks separated by 1 Hz for Goldstone and 0.28 Hz for Arecibo; those intervals correspond to a radial velocity difference of 18 mm s^{-1}. Gray scales were designed to show the extent of the delay-Doppler distributions.

hertz conversion factor as a function of time.

Toutatis's hour-to-hour rotational motion was barely perceptible, but day-to-day changes in the orientation of the line connecting the two lobes were obvious. During the first few days, the motion of the lobe-lobe line and naïve application of Eq. 5 suggested a rotation period between 4 and 5 days [compared with 0.1 to 1.0 days for almost all other measured ECA rotation periods (5)] and a view closer to equatorial than pole-on. For example, because the asteroid's typical overall dimension appears to be about 2 km and its typical bandwidth was about 2 Hz over most of the imaging sequence, one might gather from Eq. 5 that the POS component ($|\mathbf{W}_{app} \times \mathbf{e}|$) of $\mathbf{W}_{app}$ was roughly 90° per day (6). However, as the experiment progressed, it became increasingly difficult to identify any constant value for **W** that was consistent with the evolution of the delay-Doppler signature, and by the end of the experiment we realized that our premise of principal-axis rotation was incorrect.

According to force-free rigid-body dynamics, if the angular momentum vector **L** is not aligned with a principal axis, the body-fixed inertia ellipsoid will freely precess about **L** while **W** executes a periodic motion in the body, its direction defining a closed curve on the inertia ellipsoid (7). Let the principal axes x_1, x_2, and x_3 correspond to moments of inertia $I_1 \geq I_2 \geq I_3$. Rotation is stable only about x_1 or x_3. Convergence of **L** with x_1 generally will occur whenever energy dissipation is taking place in a quasi-rigid body (8); light curves show that such rotation is predominant among the asteroids (9). In contrast, for Toutatis, the lobes always overlap in frequency, even when they are at similar ranges, so we never see $\mathbf{W}_{app}$ normal to the longest dimension. Because $|\mathbf{W}_{sky}|$ is small compared to $|\mathbf{W}_{app} \times \mathbf{e}|$, we conclude that **W** is not normal to the asteroid's longest dimension; in fact, most of the images suggest that **W** is closer to the longest dimension than to its normal. This circumstance suggests either non–principal axis rotation or very unusual physical properties, but in the absence of information about the asteroid's shape and internal density distribution (and hence the inertia ellipsoid's shape and body-fixed orientation), it does not in itself preclude principal axis rotation.

However, other aspects of the image sequence do demonstrate variation of **W**, thereby establishing non–principal axis rotation. If **W** were constant in body-fixed and inertial frames, the similarity of the 2 and 13 December images (for which **e** differs by 110°) would require δ to be similar on each date, but that possibility is ruled out by the bandwidth collapse on 11

Table 1. Toutatis observations, ephemeris corrections, and astrometry. Goldstone image designations are the day of year followed by a two-digit index. Goldstone observations used the 70-m antenna, DSS-14, for transmission. Negative image designations indicate bistatic observations, done by transmitting continuously from DSS-14 and receiving at DSS-13, a 34-m antenna 22 km away. Arecibo observations were monostatic. For each image in this paper we give Toutatis's right ascension (RA), declination (DEC), distance, and rate of sky motion ($|\mathbf{W}_{sky}|$) at a UTC epoch (t_0) near the midpoint of data reception; *N* is the number of looks summed. The frequency resolution Δf has a radial-velocity equivalent of $\Delta f/2$ wavelengths per second and a length equivalent of Δf times the kilometers-per-hertz conversion factor from the Hudson-Ostro (*14*) model. For Arecibo, the data processing introduced high correlation between adjacent frequency cells. Delay-Doppler ephemeris 27*N* was calculated on 27 November, 2D on 2 December, etc. $\Delta\nu_{eph}$ and $\Delta\tau_{eph}$ are model-based (*14*) COM corrections to the specified ephemeris. Astrometry corresponds to echoes received at t_0 from Toutatis's COM. For DSS-13 and DSS-14, the reference point is the intersection of the azimuthal and elevation axes.

Date (Dec 1992)	t_0 (hh: mm)	Image	*N*	Δf (Hz)	km/ Hz	$\Delta f \times \Delta t$ (m × m)	RA (deg)	DEC (deg)	Dist. (AU)	$\lvert\mathbf{W}_{sky}\rvert$ (°/d)	Eph.	$\Delta\nu_{eph}$ (Hz)	$\Delta\tau_{eph}$ (μs)	Time delay (s ± μs)	Doppler frequency (Hz ± Hz)
Goldstone (8510-MHz, 3.5-cm) low-resolution (Δt = 500 ns) images (Fig. 1)															
2	21:40	33707	7	0.100	0.96	96 × 75	262	−32	0.042	5.3	27N	−15.75	−2009.69	42.180312122 ± 0.65	523514.760 ± 0.13
3	19:30	33804	14	0.100	0.86	86 × 75	256	−33	0.038	6.7	2D	−1.15	20.63	37.450923337 ± 0.36	494766.019 ± 0.07
4	18:10	33904	14	0.100	0.85	85 × 75	248	−33	0.033	8.6	2D	−8.04	74.80	32.975711079 ± 0.41	443775.732 ± 0.08
5	17:30	34003	18	0.100	0.89	89 × 75	237	−33	0.029	11.0	4D	1.03	76.59	29.027804001 ± 0.30	362243.902 ± 0.06
6	16:40	−34104	76	0.100	0.95	95 × 75	223	−31	0.026	13.6	4D	3.07	49.58	26.056497203 ± 0.23	248335.943 ± 0.04
7	17:20	−34204	83	0.100	1.12	112 × 75	207	−27	0.024	15.6	4D	−2.58	32.40	24.307305745 ± 0.61	
8	14:40	34304	25	0.100	1.37	137 × 75	194	−21	0.024	15.6	7D	−0.97	19.38	24.202819270 ± 0.12	−58768.687 ± 0.02
9	17:30	34402	9	0.100	1.77	177 × 75	179	−14	0.026	13.5	7D	−0.05	28.20	25.938862116 ± 0.34	−250054.867 ± 0.06
10	17:00	34503	6	0.100	2.88	287 × 75	169	−8	0.029	10.9	7D	0.99	23.05	28.867565808 ± 0.38	−364551.377 ± 0.07
11	09:40	34603	15	0.100	4.77	476 × 75	163	−4	0.032	9.1	7D	0.76	17.11	31.542082782 ± 0.34	−389322.673 ± 0.06
12	09:20	34703	18	0.100	2.13	213 × 75	157	0	0.036	7.1	7D	−0.30	15.23	35.939781859 ± 0.32	−450249.232 ± 0.06
13	08:10	34803	25	0.100	1.19	119 × 75	152	3	0.041	5.5	7D	−0.43	20.58	40.664482454 ± 0.41	−487485.645 ± 0.08
14	07:50	34903	30	0.100	0.93	86 × 75	148	6	0.046	4.4	7D	0.45	21.15	45.891287505 ± 0.48	−515942.546 ± 0.09
15	07:50	35002	29	0.100	0.86	86 × 75	144	8	0.052	3.5	7D	0.87	14.10	51.433656661 ± 0.59	−537151.849 ± 0.11
16	07:10	35104	18	0.100	0.86	86 × 75	142	9	0.057	2.9	7D	−0.58	10.64	56.997841703 ± 0.80	−550720.993 ± 0.16
17	06:50	35204	27	0.100	0.90	86 × 75	140	11	0.063	2.4	7D	−2.05	25.79	62.767761168 ± 0.84	−561924.364 ± 0.16
18	07:10	35304	151	0.100	1.15	86 × 75	138	12	0.069	2.0	7D	−0.82	45.42	68.800974112 ± 0.47	−572657.338 ± 0.09
Goldstone (8510-MHz, 3.5-cm) high-resolution (Δt = 125 ns) images (Fig. 2)															
5	18:50	34006	22	0.083	0.89	74 × 19	236	−32	0.029	11.2	4D				
6	17:30	−34107	104	0.083	0.95	79 × 19	223	−31	0.026	13.7	4D				
8	16:40	−34307	106	0.033	1.39	46 × 19	193	−21	0.024	15.6	7D				
9	17:50	−34403	25	0.033	1.78	59 × 19	179	−14	0.026	13.4	7D				
10	17:20	−34504	72	0.033	2.90	96 × 19	169	−8	0.029	10.9	7D				
11	10:30	−34605	106	0.033	4.85	161 × 19	163	−4	0.032	9.1	7D				
13	09:10	−34805	162	0.033	1.77	39 × 19	152	3	0.041	5.5	7D				
14	09:00	−34906	99	0.033	0.92	30 × 19	148	6	0.046	4.4	7D				
Arecibo (2380-MHz, 13-cm, Δt = 200 ns) images (Fig. 1)															
14	09:00		36	0.012	3.27	41 × 30	148	6	0.046	4.4	8D				
15	08:30		53	0.012	3.30	41 × 30	144	8	0.051	3.5	8D				
16	08:10		8	0.012	3.08	38 × 30	142	9	0.051	2.9	8D				
17	08:00		56	0.012	3.23	40 × 30	140	11	0.063	2.4	8D				
18	07:50		47	0.012	4.09	51 × 30	138	12	0.069	2.1	8D				
19	07:30		46	0.012	5.67	70 × 30	136	13	0.075	1.8	8D	−0.26	−2.72		

December, only 13° from the 13 December position. Also, the 11 December bandwidth is about half of that in either adjacent image, although the asteroid's direction was changing by only 7° from day to day. If all other factors were equal and if **W** were constant in body-fixed and inertial frames, then the twofold change in bandwidth within a 7° excursion in **e** would imply that $\mathbf{W}_{app}$ was about 7° from the LOS on 11 December. If we take 2 km as an upper bound on the asteroid's POS extent normal to $\mathbf{W}_{app}$ during these dates, then $|\mathbf{W}_{app} \times \mathbf{e}|$ was at least 17° per day on 11 December and twice that on the adjacent dates. Because $|\mathbf{W}_{sky}|$ was only 7° per day, the bandwidth collapse on 11 December must have been caused primarily by the collapse of $|\mathbf{W} \times \mathbf{e}|$, which in turn could mean either that $|\mathbf{W}|$ was much smaller than on dates far from 11 December (that is, the magnitude of **W** varies) or that **W** was very close to the lobe-lobe line on 11 December. However, because the lobe-lobe line itself rotated from day to day through most of the rest of the sequence, the latter possibility would mean that the body-fixed direction of **W** varies. Hence, the image sequence cannot be reconciled with a spin vector that is constant in inertial and body-fixed frames.

Table 2. Toutatis's orbital elements and 3σ uncertainties (in parentheses, in units of the last decimal places), estimated with JPL planetary ephemeris DE 245 and confirmed with ephemeris PEP740 from the Center for Astrophysics, using our radar astrometry (Table 2) and over 400 optical astrometric observations from 1988 through April 1993. Angular orbital elements are referred to the mean ecliptic and equinox of J2000. Weighted rms residuals are 0.83 arc sec, 0.087 Hz (1.5 mm s^{-1} in radial velocity) and 0.39 μs (59 m in range). TDB, barycentric dynamical time.

Epoch (TDB)	13.0 Nov 1996
Perihelion passage time (TDB)	11.04640(2) Nov 1996
Perihelion distance (AU)	0.920615832(13)
Eccentricity	0.634085830(5)
Argument of perihelion (degrees)	274.45243(135)
Longitude of ascending node (degrees)	128.64567(135)
Inclination (degrees)	0.46751(1)

Burns (*10*) argued that for plausible asteroid shapes in non–principal axis rotation, the time scale for precession of the inertia ellipsoid about **L** will be within a factor of 10 of the "rotation" time scale (the period of **W**'s body-fixed motion). That those time scales are on the order of days for Toutatis is suggested by visual inspection of Fig. 1 and the above analyses. Because the time scale for damping such slow non–principal axis rotation exceeds the age of the solar system (*9*, *11*), Toutatis's spin state might be primordial. Regardless of when it was acquired, Toutatis's rotation offers a modern-day, slow-motion example of post-collision rotation states likely to have characterized most asteroids (*12*).

Detailed definition of Toutatis's spin state (and shape) requires inversion (*13*) of the image sequence with a comprehensive physical model. Hudson and Ostro (*14*) have carried out such an inversion on the Goldstone images in Fig. 1 and the 19 December Arecibo image, and we use some of their results here. The model-based ephemeris corrections $\Delta\tau_{eph}$ and $\Delta\nu_{eph}$ (Table 1) yield astrometry that has been used to refine the asteroid's orbit (Table 2); Toutatis will pass 0.010360 AU (4 lunar distances) from Earth on 29 September 2004, the closest approach predicted for any asteroid or comet between now and 2060 (*15*). The corrections also have been used to de-smear high-resolution Goldstone images, which in Fig. 2 have been dilated according to kilometers-per-hertz conversion factors from the model solution for $\mathbf{W}_{app}(t)$.

The clearest images in Fig. 2 reveal numerous craters with diameters from ~100 to ~600 m; in the delay-Doppler projection, concavities are most readily discernible near the target's limb. The surface density of 100- to 600-m craters on Toutatis does not appear to be radically lower than that on asteroids 951 Gaspra (*16*) or 243 Ida (*17*) or on Ida's satellite Dactyl (*18*). Inversion of our highest resolution images should define the crater distribution in detail.

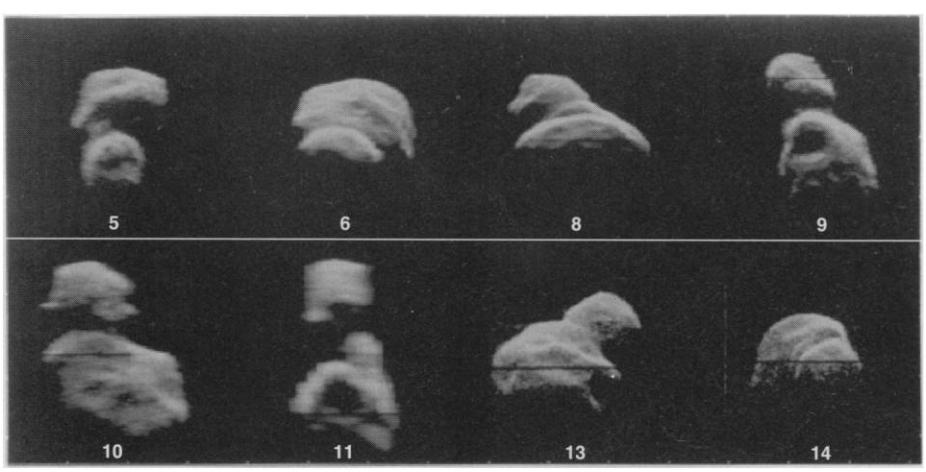

Fig. 2. High-resolution Goldstone images (*3*) of Toutatis from the indicated December dates, dilated according to kilometers-per-hertz conversion factors predicted by the Hudson-Ostro model (*14*) for the asteroid's spin state, with look-to-look translational smearing removed according to the model-based estimates of $\Delta\nu_{eph}(t)$ for each date (Table 1 and Eq. 5). Geometry is as in Fig. 1. Perimeter ticks are 1 km apart and gray scales were designed to emphasize brightness contrast.

REFERENCES AND NOTES

1. S. J. Ostro *et al.*, *Science* **248**, 1523 (1990).
2. S. J. Ostro, *Rev. Mod. Phys.* **65**, 1235 (1993).
3. Echo "self noise" dominates background receiver noise in our images.
4. The transmission was circularly polarized and echoes were received in the opposite-circular polarization. Images obtained in the same-circular polarization were similar to, but weaker than, their opposite-circular counterparts.
5. C. R. Chapman, A. W. Harris, R. P. Binzel, in *Hazards Due to Comets and Asteroids*, T. Gehrels, Ed. (Univ. of Arizona Press, Tucson, 1994), pp. 537–549.
6. The asteroid's POS motion $\mathbf{W}_{sky}$ was much slower (Table 1) and therefore had a small effect on the delay-Doppler signature over most of the imaging sequence.
7. L. D. Landau and E. M. Lifshitz, *Mechanics* (Pergamon, New York, 1976), pp. 114–120; H. Goldstein, *Classical Mechanics* (Addison-Wesley, London, 1950), pp. 143–163.
8. K. H. Prendergast, *Astron. J.* **63**, 412 (1958); R. Pringle Jr., *AIAA J.* **4**, 1395 (1966), and historical references therein.
9. A. W. Harris, *Icarus* **107**, 209 (1994).
10. J. A. Burns, in *Physical Studies of Minor Planets*, T. Gehrels, Ed. (Univ. of Arizona, Tucson, 1971), pp. 257–262.
11. J. A. Burns and V. S. Safranov, *Mon. Not. R. Astron. Soc.* **165**, 403 (1973).
12. The possibly similar rotation observed for comet Halley in 1985 probably was excited by jet-induced torques and may be very short-lived. M. J. S. Belton, W. H. Julian, A. J. Anderson, B. E. A. Meuller, *Icarus* **93**, 183 (1991); N. H. Samarasinha and M. F. A'Hearn, *ibid.*, p. 194.
13. R. S. Hudson, *Remote Sensing Rev.* **8**, 195 (1993); _____ and S. J. Ostro, *Science* **263**, 940 (1994).
14. R. S. Hudson and S. J. Ostro, *Science* **270**, 84 (1995).
15. D. K. Yeomans and P. W. Chodas, in (*5*), pp. 241–258.
16. M. J. S. Belton *et al.*, *Science* **257**, 1647 (1992).
17. M. J. S. Belton *et al.*, *ibid.* **265**, 1543 (1994).
18. C. R. Chapman *et al.*, *Nature* **374**, 783 (1995).

19. We thank the Goldstone and Arecibo technical staffs for their assistance. Part of this research was conducted at the Jet Propulsion Laboratory, California Institute of Technology, under contract with the National Aeronautics and Space Administration (NASA). The Arecibo Observatory is part of the National Astronomy and Ionosphere Center, which is operated by Cornell University under a cooperative agreement with the National Science Foundation and with support from NASA. Work at Washington State University and the Center for Astrophysics was supported in part by NASA.

4 May 1995; accepted 14 August 1995